Generalized Stability of Nongeostrophic Baroclinic Shear Flow. Part II: Intermediate Richardson Number Regime

EYAL HEIFETZ

Department of Geophysics and Planetary Sciences, Tel-Aviv University, Tel-Aviv, Israel

BRIAN F. FARRELL

Department of Earth and Planetary Sciences, Harvard University, Cambridge, Massachusetts

(Manuscript received 26 June 2006, in final form 6 March 2007)

ABSTRACT

This work continues the generalized stability theory (GST) analysis of baroclinic shear flow in the primitive equations (PE), focusing on the regime in which the mean baroclinic shear and the stratification are of the same order. The Eady model basic state is used and solutions obtained using the PE are compared to quasigeostrophic (QG) solutions.

Similar optimal growth is obtained in the PE and QG frameworks for eddies with horizontal scale equal to or larger than the Rossby radius, although PE growth rates always exceed QG growth rates. The primary energy growth mechanism is the conventional baroclinic conversion of mean available potential energy to perturbation energy mediated by the eddy meridional heat flux. However, for eddies substantially smaller than the Rossby radius, optimal growth rates in the PE greatly exceed those found in the QG. This enhanced growth rate in the PE is dominated by conversion of mean kinetic energy to perturbation kinetic energy mediated by the vertical component of zonal eddy momentum flux. This growth mechanism is filtered in QG. In the intermediate Richardson number regime mixed Rossby–gravity modes are nonorthogonal in energy, and these participate in the process of energy transfer from the barotropic source in the mean shear to predominantly baroclinic waves during the transient growth process.

The response of shear flow in the intermediate Richardson number regime to spatially and temporally uncorrelated stochastic forcing is also investigated. It is found that a comparable amount of shear turbulent variance is maintained in the rotational and mixed Rossby–gravity modes by such unbiased forcing suggesting that any observed dominance of rotational mode energy arises from restrictions on the effective forcing and damping.

1. Introduction

In the first part of this paper (Heifetz and Farrell 2003, hereafter Part I) we reported a generalized stability theory (GST) analysis of nongeostrophic baroclinic shear flow in the large Richardson number regime; that is, $\mathrm{Ri} = (N/\Lambda)^2 = O(100)$, where N is the Brunt–Väisälä frequency and Λ is the vertical shear of the mean zonal wind. This value of Ri corresponds to the typical values of stratification and baroclinic shear in the midlatitude jet [$N = O(10^{-2}\ \mathrm{s}^{-1})$; $\Lambda = O(10^{-3}\ \mathrm{s}^{-1})$]. We compared solutions obtained with the primitive equations (PE) to those obtained with the quasigeostrophic (QG) equations using the Eady (1949) basic state. For our purposes QG dynamics differs most notably from PE dynamics in filtering the divergent inertio-gravity waves while retaining the rotational Rossby waves. According to the Rossby adjustment mechanism (Blumen 1972), while an initial disturbance typically excites both rotational and inertio-gravity waves, the latter radiate quickly and presumably inconsequentially away, leaving behind the persistent rotational modes. However, this Rossby adjustment mechanism based view of the separation into rotational and divergent manifolds has been studied primarily in the absence of mean shear for which gravity and Rossby waves are orthogonal under both energy and enstrophy norms. In the presence of shear the modal solutions become mixed in divergent and rotational dynamics,

Corresponding author address: Eyal Heifetz, Department of Geophysics and Planetary Sciences, Tel-Aviv University, Tel-Aviv, Israel.
E-mail: eyalh@cyclone.tau.ac.il

DOI: 10.1175/2007JAS2225.1

and nonnormal interaction mediated growth is possible as these modes interfere in the presence of shear so that filtering out gravity waves may at the same time filter out important nonnormal growth mechanisms (cf. Duffy 1990).

Mixing between divergent and rotational modes, and the degree of nonorthogonality among modes, was found to be influenced primarily by the shear number $S = 1/\sqrt{\mathrm{Ri}} = \Lambda/N$, which is of order 0.1 for values of the Richardson number typical of mean synoptic-scale conditions. This value of S is too small to allow substantial mixing among the modes, and the Rossby modes remain almost purely rotational while the gravity modes remain almost purely divergent. Consequently, the slow Rossby manifold, the dynamics of which is described adequately by QG, remains almost orthogonal to the fast gravity manifold so that, although growth obtained with PE slightly exceeds growth obtained with QG, the PE GST analysis at synoptic time scales of several days yields almost identical results to that obtained using QG. The major difference was found in the first few hours of initial growth for which the optimal PE growth rate substantially exceeds the QG optimal growth rate. This rapid growth rate was traced to perturbations exploiting the divergent component of the meridional wind to advect the "rotational" component of the potential temperature resulting in a large transient eddy meridional heat flux. However, this growth mechanism is not sustained and therefore does not substantially affect cyclone evolution on the synoptic time scale.

We also studied optimal growth in the PE and QG at the horizontal mesoscale, $L = O(100\ \mathrm{km})$, for which $\mathrm{Ro} = O(1)$, but again keeping $\mathrm{Ri} = O(100)$. Primarily because the shear number, S, again remained too small to establish appreciable nonorthogonality between the divergent and rotational manifolds, it was found that, although the two manifolds in this regime have similar time scale, still the optimal growth for target times of a few days obtained with PE is close to that obtained with QG.

A fundamental difference between QG and PE is that QG neglects the direct mechanism of energy growth by transfer of kinetic energy from the mean shear mediated by the vertical component of zonal eddy momentum flux. This neglect is justified by the scaling of the vertical velocity in QG. However, especially at the mesoscale, this mechanism cannot always be neglected, and, in fact, we found that its contribution to the total eddy energy growth could exceed by two orders of magnitude that of the potential energy transfer mediated by meridional heat flux. Nevertheless at large Richardson number, even at mesoscale, only in the first few hours of evolution does the PE framework yield a much larger growth than the QG due to the direct Reynolds stress mechanism.

The response to stochastic forcing of PE shear dynamics was also investigated. For spatially and temporally uncorrelated forcing we found that at synoptic scale the divergent manifolds maintain a variance comparable to that maintained by the rotational manifold. In the mesoscale gravity waves maintained almost half of the total variance. While there is some observational and modeling evidence for this approximate equipartition at the mesoscale, there is no evidence for strong variance in divergent motions at synoptic scale (Errico 1984). However, when white noise was replaced by red noise, in agreement with the power-law frequency spectrum that is observed for gravity waves, the divergent variance was strongly suppressed. In addition, when the damping was made proportional to frequency (thus making the eddy decorrelation time proportional to the eddy period, a self-similarity in agreement with the observed power law spectrum) the overprediction of divergence variance was further reduced.

The results of Part I suggest that the fundamental reason the QG framework provides a good description of midlatitudinal dynamics is due as much to the smallness of the shear number as to the smallness of the Rossby number. Because the ratio of shear to stratification is small in the midlatitude jet, appreciable nonorthogonal interaction between the divergent and rotational manifolds does not occur. This result invites a study of baroclinic GST for larger shear number at various ranges of Rossby numbers, in order to identify the parameter for which the rotational and divergent manifolds mix and consequently support nonnormal growth. Hence, here in Part II, we examine nonnormal dynamics in the intermediate Richardson number regime in which $S = 1/\sqrt{\mathrm{Ri}} = O(1)$ both at Rossby numbers typical of the synoptic scale and the mesoscale [Rossby numbers $O(0.1–10)$]. This study addresses the fundamental theoretical issue of the mixing of the rotational and the divergent mechanisms in the baroclinic dynamics. Although at synoptic scale the Richardson number is usually much larger than unity, in the mesoscale an effective moist Richardson number (cf. the definition by Durran and Klemp 1982) can easily reach order one in fronts and jet streaks (e.g., Wakimoto and Bosart 2000, 2001; Bosart et al. 1998; Kaplan et al. 1997; Koch and Dorian 1988). While the dynamics discussed in this work is taken for simplicity to be dry, we expect the nonnormality dependence on the shear number is general.

In section 2 we review the baroclinic PE formulation, and in section 3 we investigate the generalized stability of the PE in the Eady basic state for the intermediate Richardson number regime. Our results and conclusions are summarized in section 4.

2. PE baroclinic dynamics

The linearized nondimensional PE, on an f plane, in the presence of constant thermally balanced zonal baroclinic shear Λ, have been written in Part I [equation set (8)]:

$$\frac{d}{dt} v_{az} = -2Sv_x + (w_x - u_{az}), \tag{1a}$$

$$\frac{d}{dt} u_{az} = 2Sv_y - (w_y - v_{az}), \tag{1b}$$

$$\frac{d}{dt} (v_x - u_y + \theta_z) = S(w_y + v_{az}). \tag{1c}$$

The zonal, meridional, and vertical directions are denoted (x, y, z) respectively. The total vector velocity perturbation is $\mathbf{u} = (u, v, w) = \mathbf{u}_a + \mathbf{u}_g$ where $\mathbf{u}_a = (u_a, v_a, w_a)$ and $\mathbf{u}_g = (u_g, v_g, 0)$ are the ageostrophic and geostrophic components. The geostrophic component satisfies the thermal wind relation $(u_{gz} = -\theta_y, v_{gz} = \theta_x)$ where θ is the scaled potential temperature;

$$\frac{d}{dt} \equiv \frac{\partial}{\partial t} + Sz \frac{\partial}{\partial x}$$

is the linearized substantial derivative, where $S = \Lambda/N = 1/\sqrt{\mathrm{Ri}}$ is the shear number and N is the Brunt–Väisälä frequency. The time scale is taken to be f^{-1}, where f is the Coriolis parameter. For the Eady basic state the tropopause height, H, provides the scale for distance in the vertical; however, there is no model constraint on the horizontal scale, L. The Rossby number is

$$\mathrm{Ro} = \frac{U}{fL} = S \frac{L_R}{L},$$

where $L_R = NH/f$ is the Rossby deformation radius and $U = \Lambda H$. We choose conventionally $L = L_R$ so that $\mathrm{Ro} = S$. However, for the same value of shear number we discuss perturbation dynamics with larger and smaller scale than the Rossby radius, which corresponds respectively to smaller and larger effective Rossby numbers. In (1) we also assumed quasi-hydrostatic balance, which requires the aspect ratio, $\alpha = H/L$, satisfy $\alpha^2 \ll 1$.

It is interesting to examine two limits of (1). In the QG limit the lhs of (1a)–(1b) and the rhs of (1c) vanish and the full horizontal wind is replaced by its geostrophic component:

$$2Sv_{g_x} = w_x - u_{az}, \tag{2a}$$

$$2Sv_{g_y} = w_y - v_{az}, \tag{2b}$$

$$\frac{d}{dt} (v_{g_x} - u_{g_y} + \theta_z) = 0. \tag{2c}$$

Equations (2a)–(2b) can be interpreted as enforcing complete adjustment to thermal wind balance in the QG framework: the horizontal thermal gradient is continuously forced by differential meridional geostrophic advection of the mean temperature [the lhs of (2a)–(2b)], which tends to violate the thermal wind balance while the ageostrophic circulation [the lhs of (2a)–(2b)] responds continuously to maintain the balance. As a result the ageostrophic dynamics is slaved to the geostrophic dynamics, which can be obtained independently by solving the geostrophic potential vorticity (PV) conservation of (2c).

The other limit is that of zero mean shear:

$$\frac{d}{dt} v_{az} = (w_x - u_{az}), \tag{3a}$$

$$\frac{d}{dt} u_{az} = -(w_y - v_{az}), \tag{3b}$$

$$\frac{d}{dt} (v_{g_x} - u_{g_y} + \theta_z) = 0. \tag{3c}$$

Equations (3a)–(3b) describe pure ageostrophic inertio-gravity wave dynamics, which is decoupled from the barotropic geostrophic dynamics of (3c) [since the inertio-gravity waves carry zero PV the only remaining PV component in (3c) is geostrophic]. The two limits are similar in the sense that the rotational geostrophic dynamics is decoupled from the divergent dynamics, while different in that the geostrophic limit does not support inertio-gravity waves. The formulation of equation set (1) indicates that coupling between the geostrophic and ageostrophic component depends on the vertical shear number, S. Imbalance between the rhs terms of (1a)–(1b) forces growth of ageostrophic vertical shear [the lhs of (1a–(1b)], while the ageostrophic terms on the rhs of (1c) produce perturbation PV by tilting horizontal mean vorticity into the vertical (Sw_y), and by tilting mean isentropes (Sv_{az}).

For typical midlatitudinal baroclinic jets $S = O(0.1)$, and therefore coupling between the geostrophic and ageostrophic manifolds is weak. Hence, in Part I, independent of the magnitude of the effective Rossby num-

ber, we found in PE a branch of rotational modes that is almost identical to that found in QG but also two branches of almost purely divergent inertio-gravity modes. It can be shown (see appendix) that under the total energy norm a purely rotational component is orthogonal to a purely divergent one. By extension an almost purely rotational mode is also almost orthogonal to an almost purely divergent mode and, consequently to the extent that modes are purely rotational or purely divergent, such modes cannot interact in a nonnormal fashion. This is why in Part I, almost no nonnormal interaction was found between the almost QG branch and the almost purely inertio-gravity modes. It is therefore important to examine the generalized stability of system (1) when the coupling is significant, that is, when the shear number is not small. Here we continue the analysis for the case in which $S = 1/\sqrt{\mathrm{Ri}} = O(1)$.

3. Intermediate Richardson number dynamics of the Eady basic state

Smaller Richardson numbers can be found in regions of strong vertical shear and/or in regions of weak stratification. Here we discuss intermediate Richardson number dynamics for various horizontal scales corresponding to the effective Rossby numbers: $\mathrm{Ro} = kS = O(0.1; 1; 10)$, where (k, l) are the zonal and meridional wavenumbers scaled by the inverse of the Rossby radius, L_R.[1] As in Part I we discuss horizontally isotropic perturbations[2] ($k = l$) and solve both the inviscid and viscid versions of (1) (for details see appendixes A and B in Part I). Despite some differences in the dynamics of the two versions for brevity we show here only the inviscid results.

a. Normal-mode analysis

The real and imaginary frequencies (ω_r, ω_i) of the modes of the discretized dynamics for $S = 1$ and for Rossby numbers $\mathrm{Ro} = O(0.1; 1; 10)$ are shown in the left panel of Fig. 1. The PE modes are denoted by the asterisks, while the two QG Eady normal modes are shown for reference by circles. In the middle panel the 149 modes are ordered increasing in their real values of frequency.[3] The fraction of mode energy in the rotational and the divergent components are indicated by the black asterisks and gray plus symbols (recall that under the quasi-hydrostatic energy norm the rotational and the divergent energy components are orthogonal and therefore their sum yields the total energy; see appendix). In the right panel, contours indicate the energy norm inner product between every pair of modes. Zero values correspond to orthogonality between modes while unity corresponds to the normalized total energy of the modes themselves (and occurs only along the diagonal of the diagrams).

In the upper left panel of Fig. 1 [$\mathrm{Ro} = O(0.1)$] three distinct branches are seen that are separated in real frequency. Growth rates of the growing and decaying modes in the middle branch are almost identical to those obtained in QG. This dispersion relation is very similar to the one obtained for the case in Part I (cf. the upper left of Fig. 4) where $S = O(0.1)$; $\mathrm{Ro} = O(0.1)$. In Part I the energy of the middle branch was found to be almost purely rotational, while the energy of the other two branches was almost purely divergent. Here, we see from the upper middle panel that, while the energy of the middle branch is also almost purely rotational, the other two branches are mixed being composed of approximately 60% divergent energy and 40% rotational energy. Therefore, as opposed to our results in Part I where the nearly divergent modes were almost orthogonal to the nearly rotational modes, here some degree of nonorthogonality between the branches is indicated in the right upper panel of Fig. 1. When $\mathrm{Ro} = O(1)$ (horizontal middle panel), the three branches are distributed continuously in frequency, but their energy partition into rotational and divergent components is almost identical to that obtained when $\mathrm{Ro} = O(0.1)$. The unstable mode growth rate is also almost identical to that in QG.

It is remarkable that the dispersion relation of the middle rotational branch is similar to the QG branch although the shear number is not small. To understand this we plot in Fig. 2 some zonal–vertical cross sections of the most unstable mode for the case [$\mathrm{Ro} = O(1)$,

[1] We use quasi-hydrostatic dynamics, which is strictly valid only for $\alpha^2 = (H/L)^2 = O[(kf/N)^2] \ll 1$. Hence, the interpretation of increasing S while decreasing N should be made keeping this quasi-hydrostatic limit in mind. As an example, for $k = 10$, $\alpha = O(10^{-3}/N)$, decreasing N by an order of magnitude from its midlatitude synoptic value [$N = O(10^{-2})$] would, strictly speaking, violate the quasi-hydrostatic assumption. Thus, geophysical interpretation of these results should be regarded as only indicative for physical situations in which the aspect ratio is not small.

[2] As shown by Stone (1966, 1970) and Plougonven et al. (2005), the modal solution depends on the ratio k/l in this regime. However, for the optimal nonmodal evolution this dependence was found to be relatively weak, except for the case where $k/l \ll 1$, which exhibits a nonmodal transient symmetric instability type of growth. The latter will be discussed in a separate paper.

[3] The Eady channel has been discretized in the vertical into 50 layers in order to obtain numerical convergence. This in turn yields 149 modes that compose the solution; for details see appendix A of Part I.

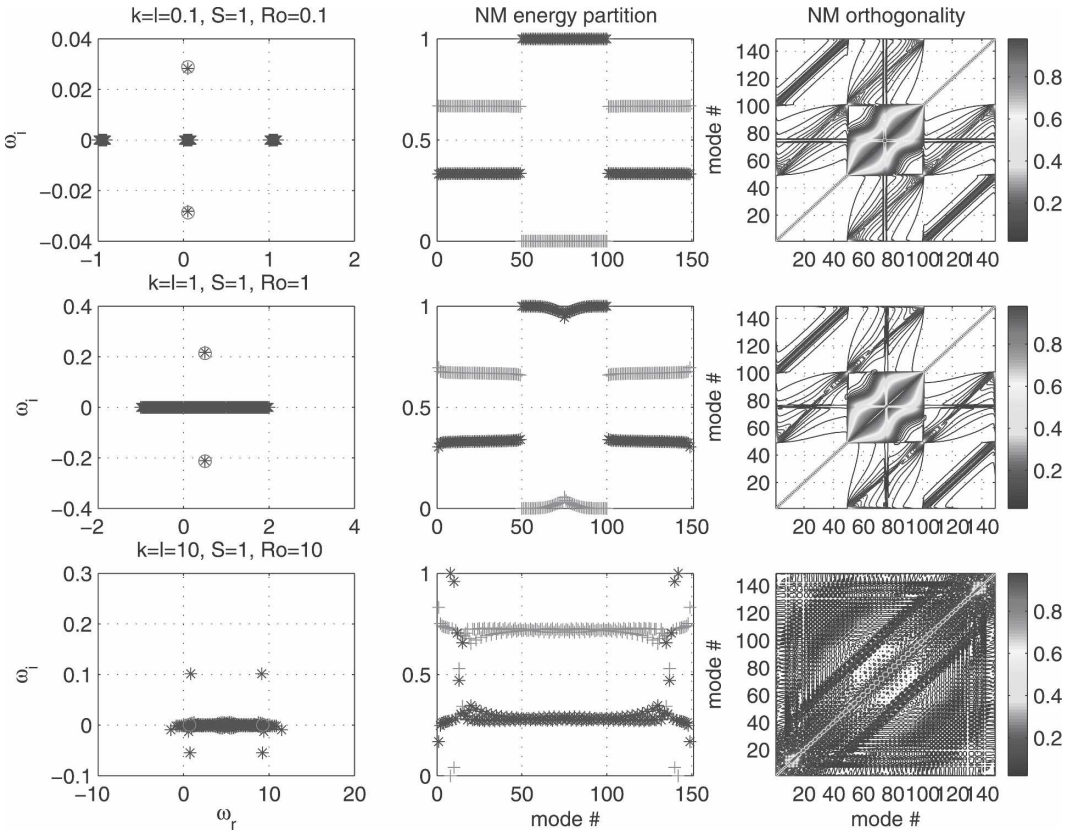

FIG. 1. (left) PE dispersion relation indicated by asterisks. The frequencies ω_r, ω_i have been scaled by the Coriolis parameter, f. The circles indicate growing and decaying normal modes obtained from QG dynamics. (middle) Partition of the modal total energy into rotational and divergent components, indicated respectively by the black asterisks and the gray plus symbols. The modes are ordered by their real frequency values so that mode 1 has the smallest real frequency. (right) Contour plot indicating the relative orthogonality among modes in the energy norm. It shows contours of $E_{i,j} = \chi_i^\dagger \chi_j$, at the intersection of ($x = i$, $y = j$), where χ_i is the normalized energy coordinate vector of mode i (ordered by their frequency values) so that $\chi_i^\dagger \chi_i = 1$: (top) $k = l = 0.1$, (middle) $l = 1$, and (bottom) $k = l = 10$.

$S = O(1)$] [the structure of the most unstable mode when Ro $= O(0.1)$, $S = O(1)$, is qualitatively similar]. In Fig. 2 the horizontal and vertical scales are normalized respectively by the wavelength and the tropopause height. The total meridional wind and its geostrophic and ageostrophic components are shown in the upper panel while the potential temperature, PV, and the vertical derivative of the ageostrophic meridional wind are shown in the lower panel. We see that all structures maximize near the boundaries. The total meridional wind is slightly tilted eastward with height, while its geostrophic component is tilted westward. The ageostrophic component is almost untilted and, in fact, looks almost identical to the first inertio-gravity mode in the Eady channel without shear. As in QG the temperature field is tilted eastward. Near the surface the meridional wind is located partly in phase and partly to the east of the temperature anomaly and thus forces the temperature anomaly to both grow and propagate eastward. Near the tropopause the meridional wind is located partly in phase and partly to the west of the temperature, forcing the latter to grow and propagate westward counter to the mean zonal eastward wind. Consequently, the mean temperature advection by the meridional wind enables the mode to resist the shear and propagate coherently eastward while growing. Unlike in QG the PE modes contain a nonzero PV anomaly that is tilted eastward with height. It can be shown that the dominant rhs term in the PV equation (1c) is Sv_{az}. Figure 2 indicates that Sv_{az}, which is almost untilted, is located near the surface partly in phase and partly to the east of the PV anomaly while partly in phase and partly to the west of the PV near the tropopause so that this differential stretching with height contributes to the

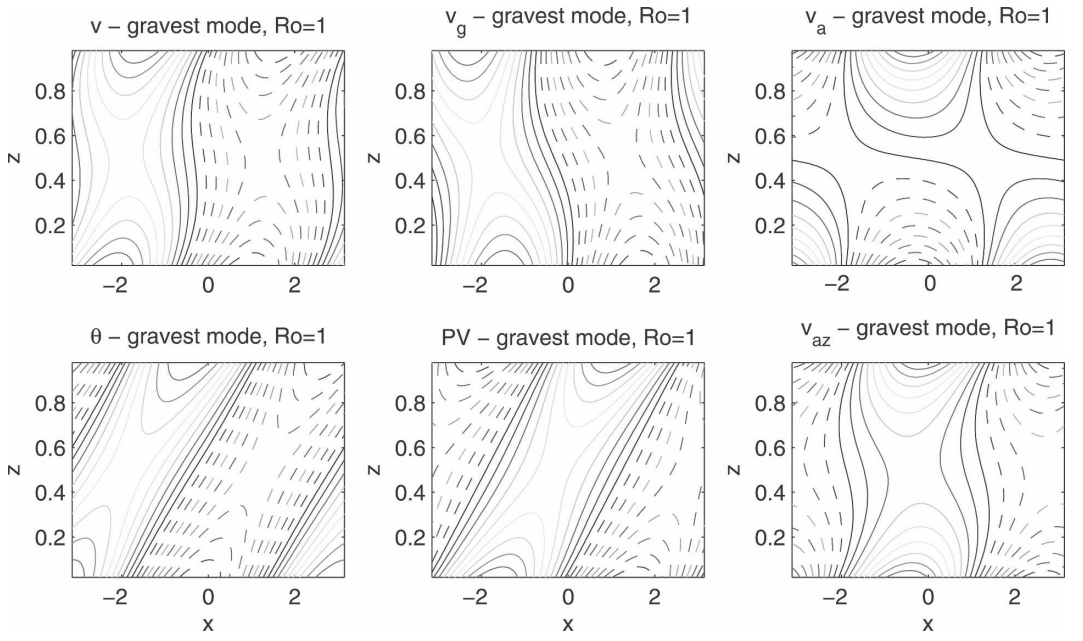

FIG. 2. Zonal–vertical cross sections of selected fields of the most unstable mode when $k = l = 1$ [Ro = $O(1)$]. The zonal direction is scaled by the eddy zonal wavelength and the vertical by the tropopause height. (top left) Total meridional wind, (top middle) geostrophic, and (top right) ageostrophic components. (bottom left) Potential temperature, (bottom middle) PV, and (bottom right) vertical derivative of the meridional ageostrophic component.

PV field propagating to the east in a coherent fashion while growing.[4]

The ratio $|v_g/v_a|$ as a function of height, indicated by the dash–dot line in the left panel of Fig. 3, is $O(1–10)$. Hence, the ratio between the geostrophic and the ageostrophic energy components might be expected to be $O(10–100)$, as indeed is verified by the solid line. Therefore, the domain-integrated ageostrophic energy is approximately 1% of the geostrophic, as was shown in Fig. 1. However, the dynamics of (1) involves the vertical derivative of the horizontal ageostrophic wind rather than the horizontal ageostrophic wind itself (the vertical wind itself contributes very little to the dynamics). A plot of the vertical distribution of $|v_g/v_{az}|$ (dashed line) shows this to be $O(10^{-1} - 1)$. Hence, although the horizontal ageostrophic wind is small compared to the geostrophic one, its vertical derivative is not. This is why the structure of the PE gravest normal mode differs substantially from its QG counterpart, although its energy remains almost purely geostrophic.

It remains to be investigated why the PE mode has almost identical growth rate to its QG counterpart despite their different structures. In normalized coordinates the quasi-hydrostatic energy tendency equation [Eq. (5) in Part I] can be written

$$\frac{\partial}{\partial t}\int \frac{1}{2}(u^2 + v^2 + \theta^2)\, dV = S\int (v\theta - uw)\, dV$$
$$= S\int [(v_g + v_a)(\theta_g + \theta_a) - (u_g + u_a)w]\, dV. \qquad (4)$$

[This partition of the ageostrophic from the geostrophic fields, including the potential temperature, was done using the QG$^+$ scheme, suggested by Muraki et al. (1999); cf. also Part I of the paper for more details.] The vertical distribution of the magnitude of the terms that compose the baroclinic energy source [the rhs of (4)] are shown in the right panel of Fig. 3. It is clear from the figure that the energy source arises predominantly from correlation between the geostrophic meridional wind and the "geostrophic" temperature components. Since the total energy of the gravest PE mode is almost geostrophic and its energy growth source is almost geostrophic as well, the resulting energy growth rate is almost that of the purely geostrophic mode.

[4] The ageostrophic circulation on the rhs of (1c) provides a source to the eddy PV and in a sense plays a role equivalent to the meridional advection of the mean interior PV in the QG framework where the mean PV gradient is nonzero, for example, the Charney (1947) model. Indeed, as in our case the PV structure of the Charney unstable modes tilt eastward with height.

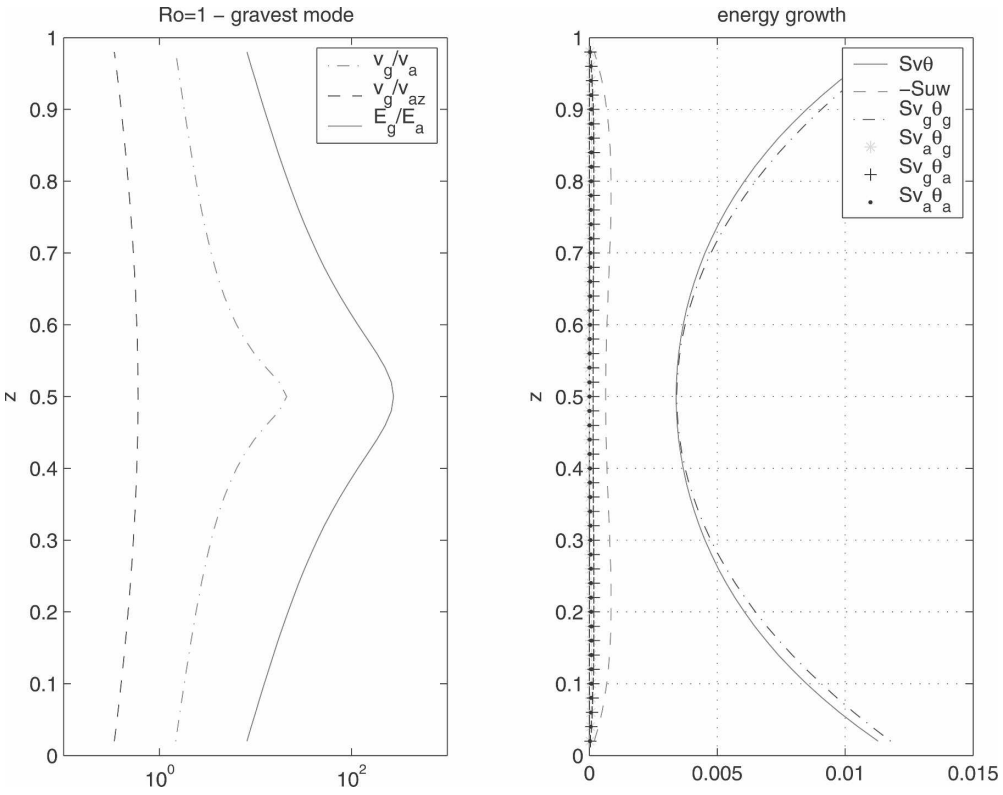

FIG. 3. (left) Vertical distribution of the ratio between selected fields of the most unstable mode when $k = l = 1$ (the vertical coordinate represents height normalized by the tropopause height). Dash–dot line indicates the ratio between the geostrophic and ageostrophic meridional wind component. Dashed line represents the ratio between the geostrophic meridional wind component and the vertical derivative of the ageostrophic meridional wind component. Solid line indicates the vertical distribution of the ratio between the geostrophic and the ageostrophic total energy. (right) Vertical distribution of the terms in the energy tendency [the rhs of (4)]. The total meridional heat flux is indicated by the solid line, while its four components ($v_g\theta_g$, $v_a\theta_g$, $v_g\theta_a$, $v_a\theta_a$) are respectively indicated by the dash–dot line, asterisk, plus, and dot symbols.

In the case with wavenumber $k = l = 10$ (lower panel of Fig. 1) so that the effective Rossby number is $O(10)$, most of the modes are mixed (middle lower panel) with energy partition of approximately 70% and 30% between the ageostrophic and geostrophic components. Therefore, the orthogonality diagnostic (right lower panel) shows some amount of nonorthogonality between almost every pair of modes (typically the degree of nonorthogonality in this inner product measure is about 30%, cf. the grayscale bar). The QG modes for this wavenumber are neutral (indicated by the circles); however, as noted by Stone (1966) and further investigated by Nakamura (1988), because of the source term in (1c), PE dynamics slightly destabilizes the modes by inducing interior critical layers. Unlike the majority of modes, these two unstable modes (number 15 and 135 in the lower panel) have almost 70% geostrophic energy and are therefore nearly orthogonal to the majority of other modes. Since the Rossby penetration depth is too small at this wavenumber to establish phase lock between the two boundary waves, these two modes remain boundary trapped critical layer instabilities, one near the surface and one near the tropopause, where their respective critical layers lie approximately at $z = 0.1; 0.9$. Cross sections of the upper unstable mode (for mode number 135) are shown in Fig. 4. We see that the structures tilt eastward with height and maximize at the upper boundary. Near the upper boundary the meridional wind is located partly in phase and partly to the west of the temperature signature producing a tendency to grow and propagate counter to the mean wind. Below the critical layer the meridional wind is partly in phase but partly to the east of the temperature field, producing a tendency to grow and propagate faster than the mean wind there. Consequently, the temperature field consistently grows while propagating coherently with the phase speed of the critical level mean wind.

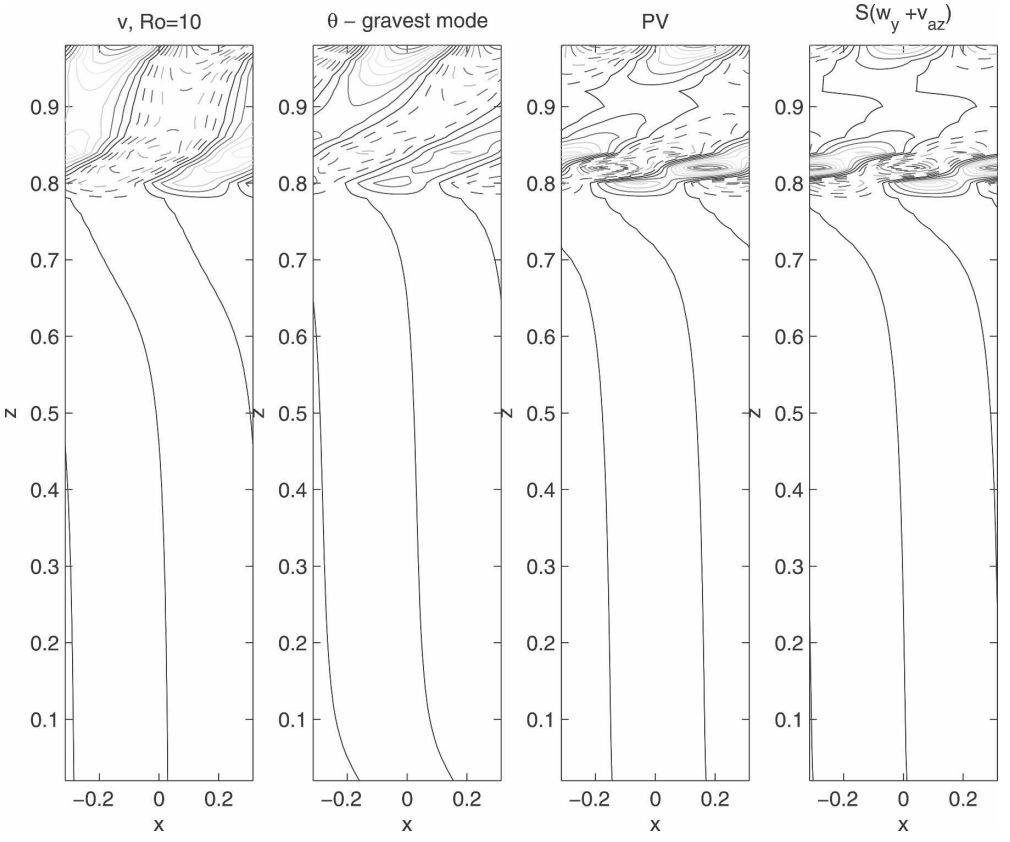

FIG. 4. Zonal–vertical cross sections of the uppermost unstable mode when $k = l = 10$ [Ro = $O(10)$]. Shown are selected fields: total meridional wind, potential temperature, PV, and the combination of ageostrophic circulation, which enter the rhs of (1c).

Having gained some familiarity with the modes we turn now from modal dynamics to explore the GST dynamics in the intermediate Richardson number regime.

b. GST analysis

Equation set (1) can be transformed into Eq. (9) of Part I:

$$\frac{\partial \boldsymbol{\chi}}{\partial t} = \mathbf{D}\boldsymbol{\chi}, \tag{5a}$$

where $\boldsymbol{\chi}$ is the generalized energy coordinates vector, whose inner product yields the quasi-hydrostatic total energy. The matrix $\mathbf{D}$ is given in appendix A of Part I. The solution of (5a) can be written

$$\chi(\mathbf{t}) = \mathbf{e}^{\mathbf{Dt}}\chi(\mathbf{0}) = \mathbf{U}\boldsymbol{\Sigma}\mathbf{V}^{\dagger}\chi(\mathbf{0}), \tag{5b}$$

where $\mathbf{U}\boldsymbol{\Sigma}\mathbf{V}^{\dagger}$ is the singular value decomposition (hereafter SVD) of the matrix propagator from an initial time zero to target time t, $\Phi(0, t) = e^{\mathbf{D}t}$ (cf. Farrell and Ioannou 1996, hereafter FI96). The optimal initial unit magnitude perturbation in the energy norm $\chi(\mathbf{0})$ producing maximal growth at target time t is the first column vector of $\mathbf{V}$, which is projected onto the first column unit vector of $\mathbf{U}$ with magnitude increase $\sigma = E_{11}$, where σ denotes the optimal growth over time t.

As in Part I we investigate first the instantaneous perturbation energy growth, continue with the optimal excitation analysis for an intermediate target time, and end this section with the optimal asymptotic limit of time infinity.

1) INSTANTANEOUS GROWTH

The maximum instantaneous growth rate of dynamical systems of the type of (5) is equal to the largest eigenvalue of the matrix $(\mathbf{D} + \mathbf{D}^{\dagger})/2$, and the structure $\boldsymbol{\chi}$ producing this growth rate is its associated eigenvector (FI96). In Fig. 1 of Part I it was shown that the PE instantaneous growth rate exceeds the QG growth rate at all wavelengths. At small wavenumbers ($k < 1$), the differences in growth rates were small because in both PE and QG the energy growth mechanism was dominated by the conventional baroclinic available potential

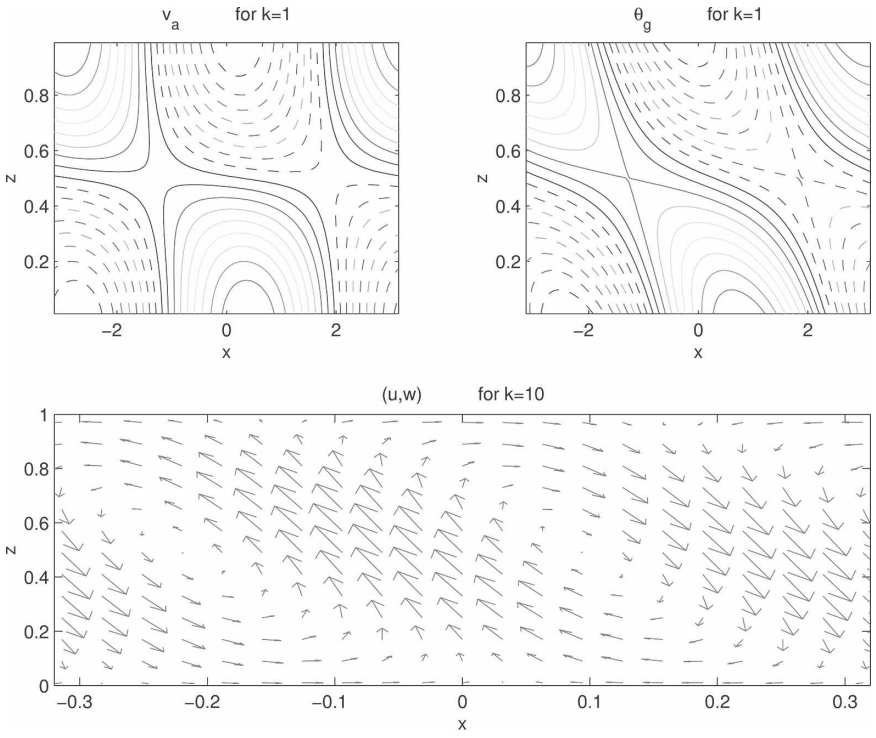

FIG. 5. Zonal–vertical cross sections of the structures with maximal instantaneous growth rate. (top left) Ageostrophic meridional wind component and (top right) "geostrophic" potential temperature when $k = l = 1$. (bottom) Scaled arrows of the (u, w) vector field for $k = l = 10$.

energy (APE) growth mechanism mediated by the eddy meridional heat flux $v\theta$. In contrast, for larger wavenumbers ($k > 2$) the differences in instantaneous growth rate are large since in the PE framework the growth is dominated by the effective kinetic energy (KE) growth, due to the zonal–vertical component of the Reynolds stress, $-uw$. The latter produces growth rates in PE that reach, at the quasi-hydrostatic limit, two orders of magnitude larger than QG growth rates. These results were found to be insensitive to the Richardson number over the range $O(10^{-4}) \leq \mathrm{Ri} \leq O(10^{4})$. Structures producing maximum instantaneous growth rate are shown in Fig. 5 for $S = 1$ and $k = 1$ (upper panel) and for $k = 10$ (lower panel). While in QG v and θ are the zonal and vertical derivatives of the geostrophic streamfunction, here for $k = 1$, PE dynamics exploits the additional freedom to amplify the meridional heat flux by advecting the "geostrophic" potential temperature with the ageostrophic meridional wind so that the volume integral of $v_a\theta_g$ in the rhs of (4) dominates the growth (cf. the remarkable correlation between the two fields in Fig. 5). The scaled vectors of the zonal and vertical wind components are also shown for $k = 10$ in Fig. 5 revealing the tilt against the mean shear indicative of energetically positive contribution from the eddy Reynolds stress, $-uw$.

The optimal instantaneous structures can be compared to the most unstable normal modes (Figs. 2–5). The most unstable modes act to maximize the correlation between v and θ under the constraint of being phase locked, and for wavenumbers corresponding to scales smaller or of order Rossby radius these fields are nearly identical to the geostrophic components of v and θ. The instantaneous structures are fundamentally different since without the phase locking constraint the structures maximize the correlation between fields, which produces maximum growth rate: however, we find that this correlation is not necessarily sustained.

In Part I we found for $S = 0.1$ that, indeed, these large instantaneous growth rates were not sustained and the intermediate time PE optimal growth was nearly the same as that in QG. We now examine the intermediate time optimal growth for $S = 1$.

2) INTERMEDIATE TIME OPTIMAL GROWTH

Finite-time optimal growth diagnostics for consecutive target times of 1 to 24 h for $S = 1$ are shown in

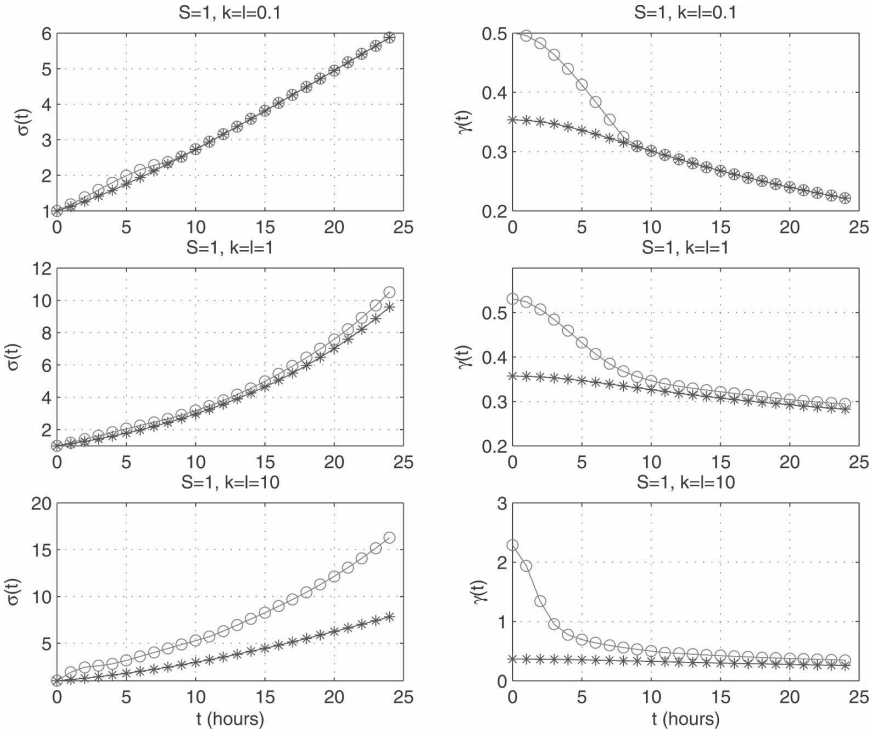

FIG. 6. (left) The optimal growth, $\sigma(t)$, obtained over time interval t by symmetric wavenumber and (right) the corresponding effective growth rate $\gamma(t) = \ln\sigma(t)/t$, scaled by $(f/N)\Lambda$. For both left and right panels the PE growth is indicated by circles, and the QG growth by asterisks. The growth corresponds to wavenumbers (top) $k = l = 0.1$, (middle) $k = l = 1$, and (bottom) $k = l = 10$.

Fig. 6. Circles indicate the PE solution and asterisks indicate the QG solution. The optimal growth $\sigma(t)$ over the interval of time t is shown in the left panel. The mean growth rate $\gamma(t)$, which solves $\sigma(t) = \exp(\gamma t)$, is shown in the right panel.[5] The upper, middle, and lower panels represent the respective growth of symmetric perturbations ($k = l$) with Ro = $O(0.1, 1, 10)$ corresponding to the respective horizontal scale of (10, 1, 0.1) times the Rossby radius. In all three cases the PE optimal growth is larger or equal to the QG growth. We can see that for very large horizontal perturbation (upper panel) the PE and the QG optimal growth are very similar and are practically the same after 8 h of evolution. For Rossby radius scale perturbation (middle panel) the PE growth always exceeds the QG but only by a little. Only in the sub-Rossby radius scale (lower panel) do the two optimal dynamics diverge significantly.

Optimal structures and energy source terms for target time 12 h (associated with the typical time scale of explosive cyclogenesis) are shown in Fig. 7. The optimal meridional wind structures are shown in the left panel and the resulting wind structures after 12 h of evolution are shown in the middle column. After 12 h, for the largest horizontal scale the structures are almost identical to those obtained in QG (in agreement with Fig. 6). At the Rossby radius scale, the structures are qualitatively similar to the QG with the initial perturbation evolving from concentration in the midtroposphere toward the upper and lower boundaries. For the sub-Rossby radius scale, the perturbation is initially tilted against the shear and is subsequently rotated by the shear (in time the perturbation converges to a superposition of the two unstable edge modes). The total energy growth rate of the 12 h optimal perturbations as a function of time is indicated by circles in the right panel. This growth rate results from the meridional heat flux contribution $v\theta$, indicated by asterisks, and the zonal–vertical Reynolds stress component $-uw$, indicated by the plus symbols. In the large horizontal scale case the total energy growth is almost solely due to the $v\theta$ term while at the Rossby radius scale it still domi-

[5] Note that $\gamma(t = 0)$ is equal to the maximum instantaneous growth rate, that is, to the largest eigenvalue of the matrix $(\mathbf{D} + \mathbf{D}^{\dagger})/2$. A comparison between these values and the values of ω_i in Fig. 1 shows that the instantaneous growth rate always exceeds the most unstable mode growth rate, as expected.

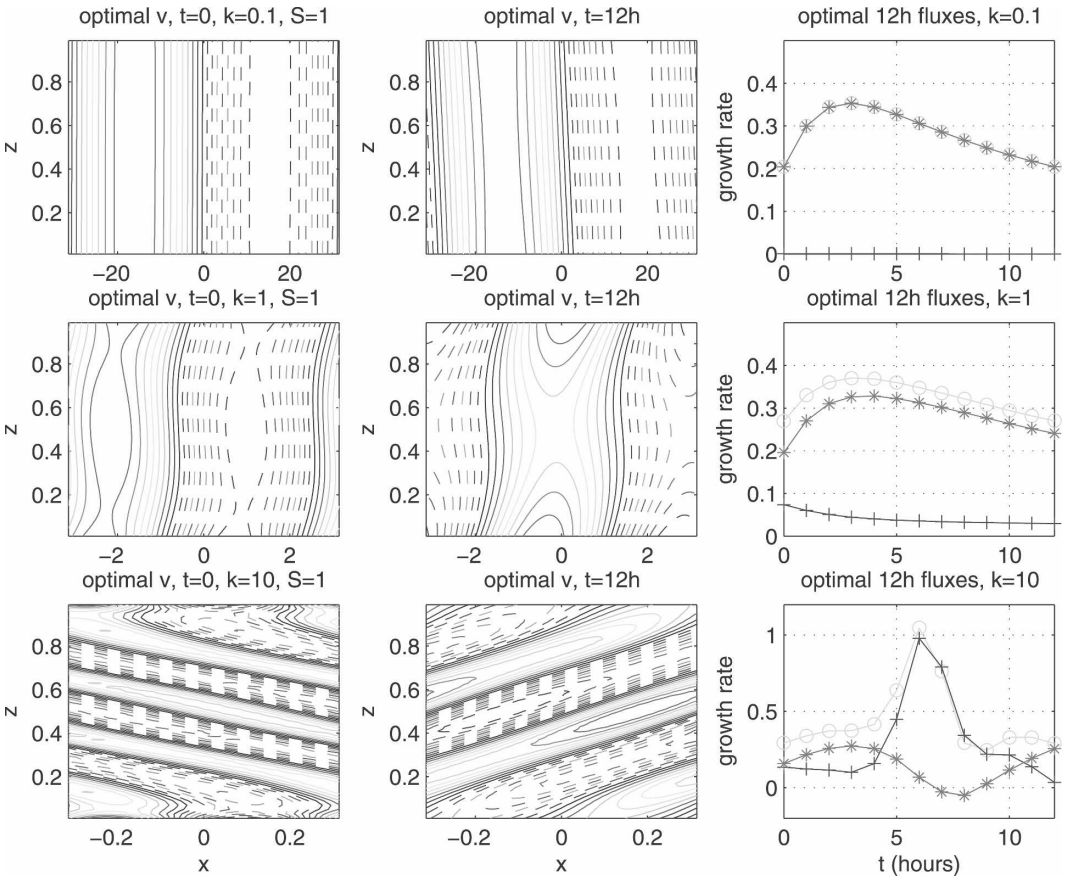

FIG. 7. (left) Zonal–vertical cross sections of the total meridional wind for the initial optimal structures for target time of 12 h. (middle) The resulting structures after 12 h. (right) Evolution of the total energy growth rate within the 12 h is indicated by the circles. The partition of this growth rate to the meridional temperature flux component and to the zonal–vertical component of the Reynolds stress are indicated respectively by the asterisks and the plus symbols. The structures and growth rates correspond to wavenumbers (top) $k = l = 0.1$, (middle) $k = l = 1$, and (bottom) $k = l = 10$.

nates the growth. Consistently, for these eddy scales the optimal PE and QG growth are similar. In contrast, in the sub-Rossby radius scale, the optimal growth is mainly due to the KE growth term $-uw$, which is filtered out a priori by QG and the optimal perturbation is primarily structured such as to maximize the contribution from $-uw$.

Hence, to summarize the intermediate time optimal growth for intermediate Richardson numbers, we note the following. The PE and QG yield similar optimal growth for horizontal scales larger or equal to the Rossby radius. This is true, although when $\mathrm{Ri} = O(1)$ the Rossby number is $O(1)$ for eddies with horizontal scale of the Rossby radius. In both cases the dominant growth mechanism is the same baroclinic transfer of mean APE mediated by meridional heat flux. On the other hand, it was shown in Part I that the direct KE growth mechanism dominates at small horizontal scales and can dominate baroclinic APE growth at larger scales. However, for large Richardson numbers the transient KE growth mechanism is not sustained. Here, for intermediate Richardson numbers, we find that this latter mechanism is sustained and provides much larger growth.

We next briefly examine optimal evolution for target time infinity.

3) THE ASYMPTOTIC $t \to \infty$ OPTIMAL

The optimal excitation for $t \to \infty$ is the perturbation that optimally excites the most unstable mode and this is the conjugate of the biorthogonal of this most unstable mode. The meridional wind structures of the most unstable modes for wavenumbers $k = 0.1, 1, 10$ are shown in the right panels of Fig. 8, while in the left

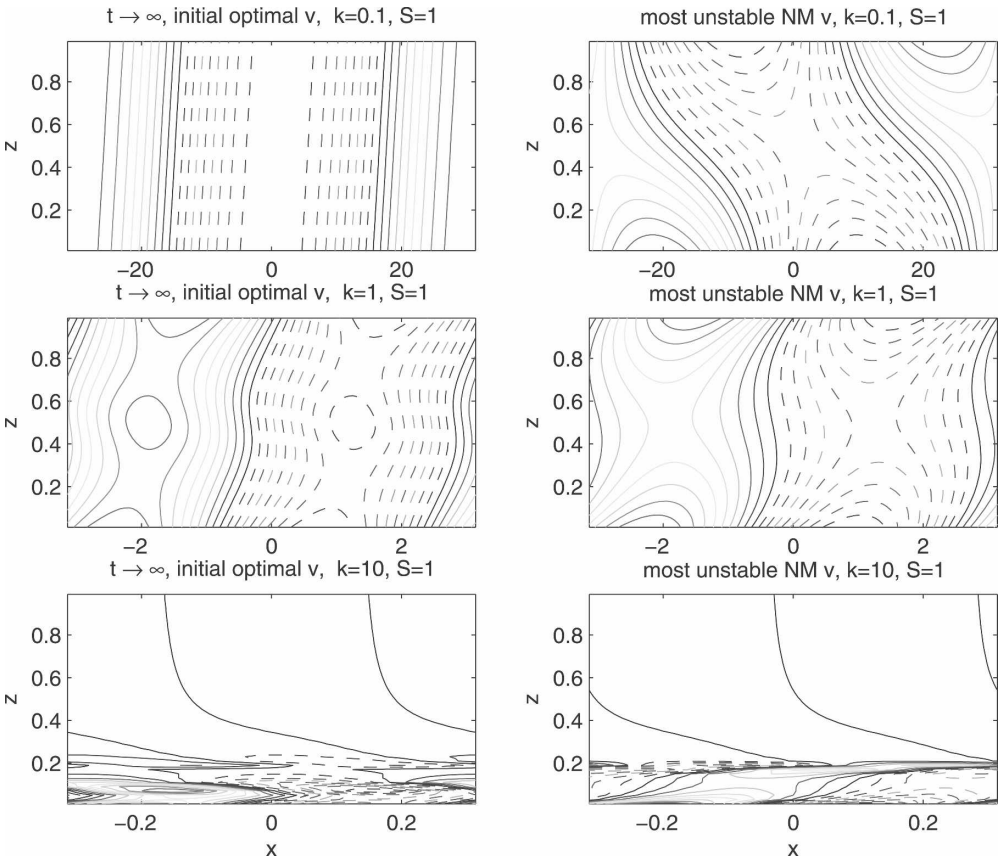

FIG. 8. (left) Zonal–vertical cross sections of the meridional wind v, for the (left) optimal and the (right) evolved optimal for target time infinity for (top) $k = l = 0.1$, (middle) $k = l = 1$, and (bottom) $k = l = 10$.

panels the optimals are shown. (Since two most unstable modes with identical growth rates exist for $k = 10$, we use this opportunity to plot in the lower panels of Fig. 8 the surface unstable mode and its biorthogonal conjugate, as the tropopause unstable mode was already shown in Fig. 4.) For $k = 0.1$ the structures are almost identical to the QG ones. The optimal QG evolution in the Eady model is investigated in detail by Morgan and Chih-Chieh (2002) and also by deVries and Opsteegh (2005). In contrast, and as in the case of the inviscid Orr–Sommerfeld equation, the optimal perturbation for $k = 1, 10$ are concentrated in the region of the critical level (Drazin and Reid 1981), where in accordance with the analysis in section 3a, their meridional wind (which is composed of both geostrophic and agestrophic components) tilt eastward with height.

In Part I we saw that although at synoptic time scales optimal dynamics in PE was similar to that in QG (Morgan and Chih-Chieh 2002; deVries and Opsteegh 2005), response to stochastic forcing was rather different in the two frameworks. Here, for intermediate Richardson number, we found more differences in optimal dynamics in the two frameworks, which suggests greater differences in their response to stochastic forcing.

c. *Response to stochastic forcing*

In stochastic shear turbulence theory stochastic forcing parameterizes excitation of the dominant nonnormal growth mechanisms by sources arising from both intrinsic nonlinear interaction among waves in the flow as well as extrinsic processes such as latent heat release (FI96). The statistical equilibrium of the midlatitudinal troposphere has been successfully modeled as an asymptotically stable linear dynamical system subject to stochastic forcing (Farrell and Ioannou 1995; DelSole and Farrell 1995; Whitaker and Sardeshmukh 1998; Zhang and Held 1999). Here we further investigate stochastic baroclinic shear turbulence at intermediate Richardson number using the PE.

Adding a forcing vector $\mathbf{g}(t)$ to the rhs of (5a) yields

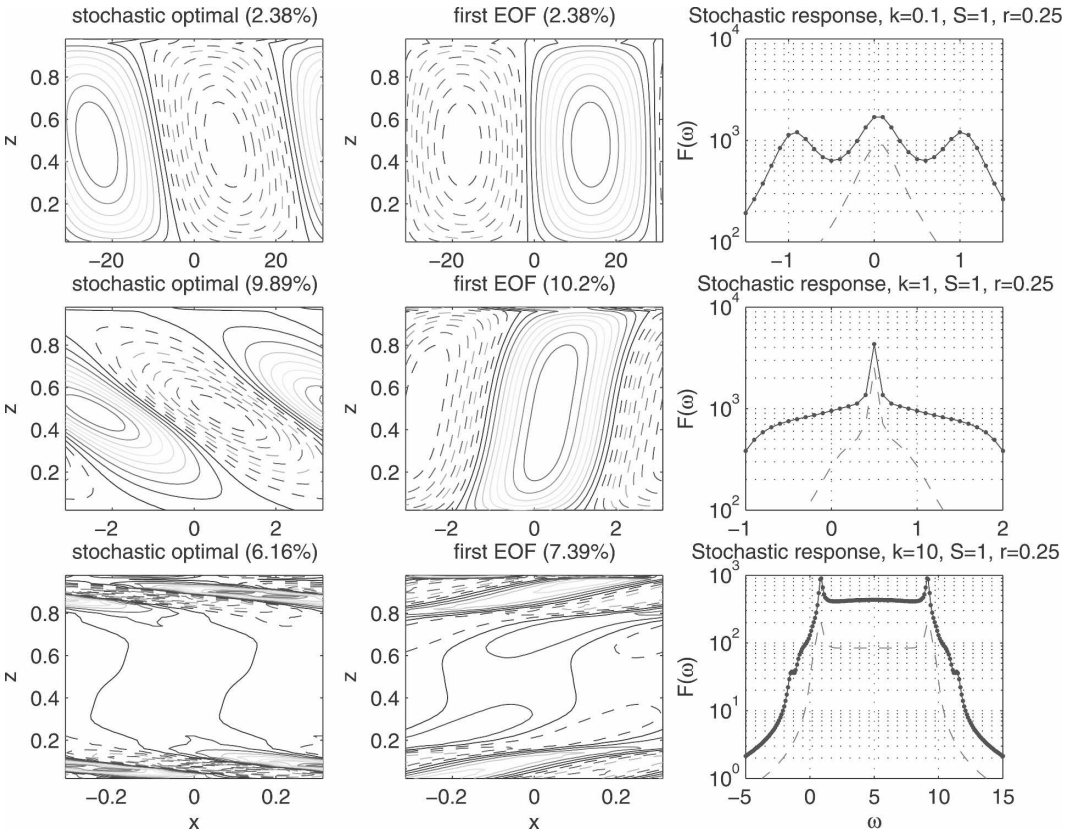

FIG. 9. The (left) first stochastic optimal and (middle) the first EOF for (top) $k = l = 0.1$, (middle) $k = l = 1$, (bottom) $k = l = 10$. In the right panels, the PE and QG frequency responses to white noise forcing are indicated by the solid dot lines and by the dashed line, respectively.

the asymptotic equilibrium solution in the frequency domain:

$$\hat{\boldsymbol{\chi}}(\omega) = \hat{\mathbf{R}}(\omega)\hat{\mathbf{g}}(\omega), \quad \hat{\mathbf{R}}(\omega) = (i\omega\mathbf{I} - \mathbf{D})^{-1}, \quad \text{(6a,b)}$$

in which the caret superscript denotes the Fourier transform,

$$\hat{\boldsymbol{\chi}}(\omega) = \frac{1}{2\pi}\int_{-\infty}^{\infty} \boldsymbol{\chi}(t)e^{-i\omega t}\,dt, \quad (7)$$

where ω is the frequency and $\mathbf{I}$ the identity matrix. Hereafter we omit the caret superscript, which indicates the frequency domain. When a spectrum of frequencies, $\omega \in (\omega_1, \omega_2)$, is excited by spatially and temporally uncorrelated forcing with unit variance, that is, $\langle \hat{\mathbf{g}}_i(\omega_m), \hat{\mathbf{g}}_j^*(\omega_n)\rangle = \delta_{ij}\delta(\omega_m - \omega_n)/2\pi$, the ensemble variance resulting is given by

$$\langle \boldsymbol{\chi}^2 \rangle = \frac{1}{2\pi}\int_{\omega_1}^{\omega_2} F(\omega)\,d\omega, \quad (8)$$

where $F(\omega) = \text{trace}[\mathbf{R}^\dagger(\omega)\ \mathbf{R}(\omega)]$. The frequency response $F(\omega)$ is shown in Fig. 9 for the three horizontal wavenumbers $k = 0.1, 1, 10$ and in the presence of equal Rayleigh damping and Newtonian cooling, corresponding to a 1-day damping time. While this is an overestimation of the explicit damping in the atmosphere, within the context of stochastic turbulence theory it accounts for both linear and nonlinear damping mechanisms serving to limit perturbation growth. That these damping mechanisms in total are equivalent to the damping rate assumed is required by boundedness or turbulent variance, as this damping ensures that all modes decay and consequently $F(\omega)$ is bounded. The PE response is larger than the QG at all frequencies, and most notably the PE response is substantial at high frequency for which the QG response is negligible.

For spatially and temporally uncorrelated forcing the EOFs and the stochastic optimals are obtained respectively by SVD of the matrices $\mathbf{C}$, $\mathbf{B}$:

$$\mathbf{C} = \frac{1}{2\pi}\int_{\omega_1}^{\omega_2} \mathbf{R}(\omega)\mathbf{R}^\dagger(\omega)\mathbf{d}\omega; \quad \mathbf{B} = \frac{1}{2\pi}\int_{\omega_1}^{\omega_2} \mathbf{R}^\dagger(\omega)\mathbf{R}(\omega)\mathbf{d}\omega, \quad \text{(9a,b)}$$

with **C** and **B** obtained conveniently by solving the algebraic Lyapunov equations:

$$\mathbf{DC} + \mathbf{CD}^{\dagger} = -\mathrm{I}; \quad \mathbf{D}^{\dagger}\mathbf{B} + \mathbf{BD} = -\mathbf{I}. \quad (10a,b)$$

The structures of the first stochastic optimal and the first EOF are plotted respectively in the left and middle columns of Fig. 9 for $k = l = 0.1$. From the right upper panel we see that variance is distributed almost equally among the three branches of predominantly rotational modes (middle branch) and the two mixed Rossby–gravity branches. This distribution was also obtained in Part I in the large Richardson number regime. Using (9) we can find **C** and **B** for each branch separately and obtain the first stochastic optimal and first EOF for each branch separately. For the rotational branch these structures (not shown here) are similar to the optimal for target time infinity and to the most unstable mode (cf. upper panels of Fig. 8). For the mixed branches the structures were found to be statistically degenerate. For $k = l = 1$ the variance is maximized for the rotational unstable mode (which becomes the least damped mode in the presence of damping); however, the distribution of the response in the mixed range is rather uniform. The first stochastic optimal displays a tilted-against-the-shear structure concentrated in the midtroposphere, and the first EOF a more vertical structure tilted slightly with the shear. For the case of $k = l = 10$, the first EOF shown in the middle lower panel resemble the two boundary modes. The first stochastic optimal for this case maximizes at the two critical layers of these two modes and resemble the target time infinity optimals. Both structures carry less than 8% of the total energy since the variance is distributed uniformly among the mixed modes in the frequency range $\omega \in (0, 10)$.

While the eddy baroclinic spectrum has been investigated previously in the large Richardson number regime and at synoptic scale, we are not aware of observational studies of the spectrum of motions in the intermediate Richardson number regime to which we could make comparison (cf. Errico 1984).

4. Discussion

The motivation for this study was to further understanding of the dynamics of eddies in baroclinic jets. The baroclinic basic state is highly nonnormal and implications of this nonnormality for dynamics have been investigated primarily in the QG framework or at synoptic scale (e.g., Farrell 1984; Farrell and Ioannou 1995, 1996; DelSole and Farrell 1995; Whitaker and Sardeshmukh 1998; Zhang and Held 1999). We suspected that such analysis might be incomplete since QG is based on assumptions that rule out specific growth mechanisms and, while modal baroclinic PE instability has been investigated extensively (e.g., Árnason 1963; Stone 1966, 1970; Derome and Dolph 1970; Mak 1977; Bannon 1989; Nakamura 1988; Snyder 1995; Yamazaki and Peltier 2001), we speculated that PE nonnormal dynamics might differ from QG dynamics in ways not revealed by modal analysis.

PE dynamics differs from QG by including explicitly the divergent dynamics that give rise to direct kinetic energy growth mechanisms via the zonal–vertical component of the Reynolds stress. The filtering out of divergent modes by QG is based on temporal scale separation and is justified by the smallness of the Rossby number. The neglecting of the KE growth mechanism is based on the eddies horizontal scale, which is assumed to be of the order of the Rossby radius of deformation.

At first consideration it might seem that neglect of divergent dynamics should not greatly affect optimal PE solutions since purely divergent modes and purely rotational modes are orthogonal under both energy and enstrophy norms and therefore do not interact in a nonnormal fashion. However, in the primitive equations mixing of rotational and divergent components within the modes depends on the magnitude of the shear number. In Part I we examined the optimal dynamics for shear number of order 0.1 (Richardson number of order 100) since this value is typical of the midlatitudinal baroclinic jet. It turned out that for this value of shear number there is little mixing of divergent and rotational components within the modes. Consequently the almost purely rotational modes are almost identical to the QG modes while additionally there are a set of divergent modes that are almost identical to the inertio-gravity modes. As a result, optimal growth at synoptic time scale is almost identical in the two frameworks. The KE growth mechanism at horizontal scales smaller than the Rossby radius is also not sustained although it is large initially.

In Part II we investigated baroclinic shear dynamics at intermediate Richardson number (where both the shear and the Richardson numbers are at the order of 1) hypothesizing that here the explicit divergent dynamics would have more effect on the optimal evolution. Such Richardson numbers are found in regions of strong shear and weak stratification such as in jet streaks and fronts.

We found that for horizontal scales equal to or larger than the Rossby radius modes have frequency and growth rates almost identical to QG modes although

the shear number is not small. Consistently, the energy of these modes is almost purely rotational. The major difference in the two frameworks is that the energy of the set of modes in PE not found in QG consists of a mixture of approximately 60% divergent and 40% rotational energy. While PE modes are not identical to their QG counterparts, their growth rates are practically the same. Their growth is due to the conventional available potential energy conversion from the basic state mediated by the eddy meridional heat flux. These results secure and extend QG validity to nonnormal dynamics in the intermediate Richardson number regime for eddies that are larger or equal to the Rossby radius.

For eddies with smaller scale than the Rossby radius a different picture emerges. Most modes are mixed, comprising approximately 70% divergent and 30% rotational energy. Furthermore, the PE introduced additional trapped boundary unstable modes, which were approximately 70% rotational and 30% divergent. The growth mechanism of these Rossby–gravity modes was found to be primarily the conventional APE conversion. In contrast, the nonorthogonality between the modes allowed the PE optimal evolution to take advantage of the KE growth mechanism to provide a much larger growth than obtained in QG by the APE mechanism. Thus, for sub-synoptic-scale eddies [Ro = $O(10)$] in the intermediate Richardson number regime, optimal PE growth is fundamentally different from QG growth. Therefore, the optimal structures are configured to maximize the evolution of correlation between the westward eddy's wind and its upward vertical velocity, rather than to maximize the correlation between the eddy's meridional wind and potential temperature.

It is the shear number that determines the amount of coupling between the ageostrophic and geostrophic circulations, and it is the Rossby radius that determines the horizontal scales for which the KE growth mechanism dominates the APE one. In Part I we found that for large Richardson number (small shear number) the PE optimal dynamics is close to the QG optimal dynamics for both Rossby numbers of 0.1 and 1. For Richardson (and shear) numbers of order unity the Rossby number is also of order unity if the horizontal scale is the Rossby radius, and the optimal growth was again found to be similar to that found in QG for both Rossby number values 0.1 and 1. It was the combination of the intermediate shear number (which breaks the orthogonality between the modes) and the small horizontal scale (which allows the KE growth mechanism to dominate) that enables PE dynamics to obtain much larger growth than QG.[6] The existence of an additional manifold of modes in PE might change its statistical equilibrium response to stochastic forcing. In Part I we found that for large Richardson number the synoptic-scale divergent modes carry more variance than the rotational modes when forcing was unbiased (white noise). There is no observational support for large-scale divergent eddies of this amplitude in the midlatitudes. We found that, by replacing the white noise by red and making damping linearly proportional to the frequency, the divergent variance could be suppressed, but it remains an open question why the easily excited divergent motions are not observed. For the intermediate Richardson number regime at horizontal scales larger or equal to the Rossby radius we also found that a substantial amount of variance in horizontal scales larger or equal to the Rossby radius is maintained in the mixed modes. The energy accounted for by the stochastic optimal and the first EOF are small, indicating an even partition of variance among the modes. For scale smaller than the Rossby radius the first EOF resembles the boundary modes and the stochastic optimal resembles a superposition of their biorthogonal conjugate vectors. For all three scales PE variance exceeds QG variance at all frequencies. As in the large Richardson number regime, red noise and damping linearly proportional to frequency suppressed the divergent variance but we are not aware of observational constraints on eddy variance and structure in the intermediate Richardson number regime to be used for comparison.

This analysis was carried out in the Eady basic state because of its simplicity and because both its QG nonnormal dynamics (Farrell 1984) and its PE normal dynamics (Stone 1966, 1970; Nakamura 1988; Bannon 1989; Yamazaki and Peltier 2001) have been investigated. It is possible that other dynamical effects occur when curvature and variation of the Coriolis parameter are also taken into account.

Acknowledgments. This work was supported by NSF ATM-0123389. EH is grateful to ISF 0603414721.

APPENDIX

Energy Norm Orthogonality

Applying the 3D Helmholtz decomposition, suggested by Muraki et al. (1999),

[6] For larger shear numbers $O(10)$ and Rossby numbers order unity or larger, the optimal growth were found to be primarily associated with interaction among the divergent modes. However, since this regime is remote from the primary focus of this paper on the interaction of the rotational and divergent manifolds we did not show these results.

$$\begin{pmatrix} v \\ -u \\ \theta \end{pmatrix} = \nabla\Phi + \nabla \times \boldsymbol{\zeta} = \nabla\Phi + \nabla \times \begin{pmatrix} F \\ G \\ 0 \end{pmatrix} = \begin{pmatrix} \Phi_x - G_z \\ \Phi_y + F_z \\ \Phi_z + G_x - F_y \end{pmatrix}, \tag{A1}$$

then $\nabla\Phi$ and $\nabla \times \boldsymbol{\zeta}$ represent respectively the rotational and divergent components of $(v, -u, \theta)$. We use the Fourier decomposition for the state vector

$$\boldsymbol{\eta} = \hat{\boldsymbol{\eta}}(z, t)e^{i(kx+ly)} = [\hat{\mathbf{F}}(z, t), \hat{\mathbf{G}}(z, t), \hat{\boldsymbol{\Phi}}(z, t)]e^{i(kx+ly)}, \tag{A2}$$

and the rigid horizontal boundary conditions of $w(z = 0) = w(z = 1) = 0$, which were shown in appendix A of Part I to require

$$F(0) = G(0) = 0; \quad F(1) = G(1) = 0. \tag{A3}$$

We wish to show that the rotational and divergent components are orthogonal under the quasi-hydrostatic total energy norm; that is, the energy volume integral in the Eady channel can be written as

$$\frac{1}{2}\int (u^2 + v^2 + \theta^2)\, dV = \frac{1}{2}\int |\nabla\Phi|^2\, dV + \frac{1}{2}\int |\nabla \times \boldsymbol{\zeta}|^2\, dV. \tag{A4}$$

Hence, it is left to be shown that

$$\int \nabla\Phi \cdot \nabla \times \boldsymbol{\zeta}\, dV = 0. \tag{A5}$$

Using (A1) and (A2), then

$$\int \nabla\Phi \cdot \nabla \times \boldsymbol{\zeta}\, dV = i\int_0^1 [k\hat{\boldsymbol{\Phi}}^*\hat{\mathbf{G}}_z - l\hat{\boldsymbol{\Phi}}^*\hat{\mathbf{F}}_z + \hat{\boldsymbol{\Phi}}_z^*(k\hat{\mathbf{G}} - l\hat{\mathbf{F}})]\, dz = i\int_0^1 [\hat{\boldsymbol{\Phi}}^*(k\hat{\mathbf{G}} - l\hat{\mathbf{F}})]_z\, dz = 0. \tag{A6}$$

The asterisk denotes the complex conjugate. The last integral in (A6) vanished due to the boundary conditions of (A3).

REFERENCES

Árnason, G., 1963: The stability of nongeostrophic perturbations in a baroclinic zonal flow. *Tellus,* **15,** 205–211.

Bannon, P. R., 1989: Linear baroclinic instability with the geostrophic momentum approximation. *J. Atmos. Sci.,* **46,** 402–409.

Blumen, W., 1972: Geostrophic adjustment. *Rev. Geophys. Space Phys.,* **10,** 485–528.

Bosart, L. F., W. E. Bracken, and A. Seimon, 1998: A study of cyclone mesoscale structure with emphasis on a large-amplitude inertia–gravity waves. *Mon. Wea. Rev.,* **126,** 1497–1527.

Charney, J. G., 1947: The dynamics of long waves in a baroclinic westerly current. *J. Meteor.,* **4,** 135–163.

DelSole, T., and B. F. Farrell, 1995: A stochastically excited linear system as a model for quasigeostrophic turbulence: Analytic results for one- and two-layer fluids. *J. Atmos. Sci.,* **51,** 2531–2547.

Derome, J., and C. L. Dolph, 1970: Three-dimensional nongeostrophic disturbances in a baroclinic zonal flow. *Geophys. Fluid Dyn.,* **1,** 91–122.

deVries, H., and J. D. Opsteegh, 2005: Optimal perturbations in the Eady model: Resonance versus PV unshielding. *J. Atmos. Sci.,* **62,** 492–505.

Drazin, P. G., and W. H. Reid, 1981: *Hydrodynamic Stability.* Cambridge University Press, 525 pp.

Duffy, D. G., 1990: Geostrophic adjustment in a baroclinic atmosphere. *J. Atmos. Sci.,* **47,** 457–473.

Durran, D. R., and J. B. Klemp, 1982: On the effects of moisture on the Brunt–Vaisala frequency. *J. Atmos. Sci.,* **39,** 2152–2158.

Eady, E. T., 1949: Long waves and cyclone waves. *Tellus,* **1,** 33–52.

Errico, R., 1984: The statistical equilibrium solution of a primitive equation model. *Tellus,* **36A,** 42–51.

Farrell, B. F., 1984: Modal and non-modal baroclinic waves. *J. Atmos. Sci.,* **41,** 668–673.

——, and P. J. Ioannou, 1995: Stochastic dynamics of the midlatitude atmospheric jet. *J. Atmos. Sci.,* **52,** 1642–1656.

——, and ——, 1996: Generalized stability theory. Part I: Autonomous operators. *J. Atmos. Sci.,* **53,** 2025–2040.

Heifetz, E., and B. F. Farrell, 2003: Generalized stability of nongeostrophic baroclinic shear flow. Part I: Large Richardson number regime. *J. Atmos. Sci.,* **60,** 2083–2100.

Kaplan, M. L., S. E. Koch, Y.-L. Lin, R. Weglarz, and R. A. Rozumalski, 1997: Numerical simulations of a gravity wave event over CCOPE. Part I: The role of geostrophic adjustment in mesoscale jet streak and gravity wave generation. *Mon. Wea. Rev.,* **125,** 1185–1211.

Koch, S. E., and P. B. Dorian, 1988: A mesoscale gravity wave event observed over CCOPE. Part III: Wave environment and probable source mechanisms. *Mon. Wea. Rev.,* **116,** 2570–2592.

Mak, M., 1977: On the nongeostrophic baroclinic instability problem. *J. Atmos. Sci.,* **34,** 991–1002.

Morgan, M. C., and C. Chih-Chieh, 2002: Diagnosis of optimal perturbation evolution in the Eady model. *J. Atmos. Sci.,* **59,** 169–185.

Muraki, D. J., C. Snyders, and R. Rotunno, 1999: The next-order corrections to quasigeostrophic theory. *J. Atmos. Sci.,* **56,** 1547–1560.

Nakamura, N., 1988: Scale selection of baroclinic instability—Effects of stratification and nongeostrophy. *J. Atmos. Sci.,* **45,** 3253–3267.

Plougonven, R., D. J. Muraki, and C. Snyder, 2005: A baroclinic instability that couples balanced motions and gravity waves. *J. Atmos. Sci.,* **62,** 1545–1559.

Snyder, C., 1995: Stability of steady fronts with uniform potential vorticity. *J. Atmos. Sci.,* **52,** 724–736.

Stone, P. H., 1966: On non-geostrophic baroclinic stability. *J. Atmos. Sci.,* **23,** 390–400.

——, 1970: On non-geostrophic baroclinic stability: Part II. *J. Atmos. Sci.,* **25,** 721–726.

Wakimoto, R. M., and B. L. Bosart, 2000: Airborne radar observations of a cold front during FASTEX. *Mon. Wea. Rev.,* **128,** 2447–2470.

——, and ——, 2001: Airborne radar observations of a warm front during FASTEX. *Mon. Wea. Rev.,* **129,** 254–274.

Whitaker, J. S., and P. D. Sardeshmukh, 1998: A linear theory of extratropical synoptic eddy statistics. *J. Atmos. Sci.,* **55,** 237–258.

Yamazaki, H. Y., and W. R. Peltier, 2001: On the existence of subsynoptic-scale baroclinic instability and the nonlinear evolution of shallow disturbances. *J. Atmos. Sci.,* **58,** 657–683.

Zhang, Y., and I. Held, 1999: A linear stochastic model of a GCM's midlatitude storm tracks. *J. Atmos. Sci.,* **56,** 3416–3435.